Probability density difference-based active contour for ultrasound image segmentation

Bo Liu [a], H.D. Cheng [a,b,*], Jianhua Huang [a], Jiawei Tian [c], Xianglong Tang [a], Jiafeng Liu [a]

[a] School of Computer Science and Technology, Harbin Institute of Technology, Harbin PR China
[b] Department of Computer Science, Utah State University, Logan, UT 84322, USA
[c] Second Affiliated Hospital of Harbin Medical University, Harbin PR China

ARTICLE INFO

ABSTRACT

Because of its low signal/noise ratio, low contrast and blurry boundaries, ultrasound (US) image segmentation is a difficult task. In this paper, a novel level set-based active contour model is proposed for breast ultrasound (BUS) image segmentation. At first, an energy function is formulated according to the differences between the actual and estimated probability densities of the intensities in different regions. The actual probability densities are calculated directly. For calculating the estimated probability densities, the probability density estimation method and background knowledge are utilized. The energy function is formulated with level set approach, and a partial differential equation is derived for finding the minimum of the energy function. For performing numerical computation, the derived partial differential equation is approximated by the central difference and non-re-initialization approach. The proposed method was operated on both the synthetic images and clinical BUS images for studying its characteristics and evaluating its performance. The experimental results demonstrate that the proposed method can model the BUS images well, be robust to noise, and segment the BUS images accurately and reliably.

1. Introduction

The segmentation of ultrasound (US) image is an important component of computer-aided diagnosis (CAD) system [1]. US image segmentation is to partition the image into different regions which is necessary for computer-aided diagnosis. The quality of most US images is quite poor in threefold: low signal/noise ratio (SNR), low contrast, and blurry boundaries. Hence, the US image segmentation is a difficult task. On the other hand, US imaging has become one of the most prevalent medical imaging technologies since it is non-invasive, practically harmless, and cost effective. However, the US imaging diagnosis is subjective, and its effectiveness depends on radiologist's experience and skills. Because of the above two aspects, there are more and more demands of CAD technologies in clinical applications, and developing an effective US image segmentation method becomes a pressing need.

Several segmentation methods have been published: Markov random field (MRF) [3–6], region growing [7,8], Kalman filter [9], supervised machine learning [8,10–12], multidimensional space-frequency method [13], watershed [14], cell-competition [15], fast marching [16], fuzzy logic [17], active contour [8,11,18–22], etc. Model-based approaches (MRF, active contour, etc.) have shown an advantage for handling noise. In most model-based approaches, an energy function is formulated, and the segmentation problem is transformed as finding the minimum (or maximum) of the energy function. In energy function, both image information and relationships between neighboring pixels can be integrated conveniently, therefore, model-based approaches can handle noise while utilizing image information. The quality of US image is greatly degraded by speckle noise [23,24], hence, reducing noise is essential and critical to US image segmentation. Although there are some methods for suppressing speckle noise [25–27], the trade-off between noise suppression and feature preserving is still a dilemma. Model-based approach is suitable for US image segmentation, however, the energy function needs to be well formulated.

Level set method was proposed [28] and applied to image segmentation [29]. Recently, this method was also employed for US image segmentation [30,31]. In the classical level set method, a differential equation must be formulated explicitly for evolving auxiliary level set function. However, in most cases, the explicit formulation of the evolution equation is complicated and difficult, and not convenient for modeling the problem directly.

In level set-based active contour approaches, there are usually three steps for segmentation. (1) Formulate an energy function.

* Corresponding author at: School of Computer Science and Technology, No. 352 postal box, Harbin Institute of Technology, Harbin, No. 92, Xidazhi Street, Harbin 150001, PR China. Tel.: +86 451 86413631; fax: +86 451 86413631.
E-mail address: hengda.cheng@usu.edu (H.D. Cheng).

(2) Derive an evolution equation for finding the minimum of the energy function. (3) Solve the evolution equation for obtaining segmentation result. The main difference between classical active contour approaches [32] and level set-based active contour approaches is that the level set-based active contour approaches introduce the auxiliary level set functions into the energy functions. Utilizing the level set functions, level set-based active contour models can track the evolution of the fronts in the image instead of only tracking the boundaries of the objects, and the topological variations of the boundary curves can be well handled. With this property, the level set-based active contour approaches are more effective.

Level set-based active contour models can be divided into two categories: "edge-driven" and "region-driven". For "edge-driven" models, an edge descriptor is usually calculated to find boundary curves with strong edge response [33]. For "region-driven" models, the energy function is established by considering the global information such as the mean of partitioned regions [34], the weighted mean of the constrained or scalable neighboring regions [22,35], statistical information of partitioned regions [20,36,37], etc. Comparing to "edge-driven" approach, the smooth or vanishing boundaries can be handled better by the "region-driven" approach since the information of different regions can be well considered [34]. According to the nature of US image (low SNR, low contrast, blurry boundaries, etc.), the "region-driven" approach is more suitable for modeling and solving the US image segmentation tasks.

In this paper, a novel "region-driven" level set-based active contour model is proposed for US image segmentation. Its energy function is based on the differences between the actual probability densities of the intensities in different regions and the corresponding estimated probability densities. For modeling and calculating the estimated probability densities, shifted-Rayleigh prior and probability density estimation method are utilized. The derived evolution equation is approximated with the finite difference and non-re-initialization approach. In the experiments, a series of synthetic images and breast ultrasound (BUS) images are employed for evaluating the performance of the proposed method. The experimental results demonstrate that the proposed method can segment both synthetic and clinical images accurately and effectively.

The structure of the paper is as follows. In Section 2, the proposed method is discussed. The segmentation results are shown in Section 3. A brief conclusion is presented in Section 4.

2. Proposed method

2.1. Overview of the proposed method

Considering image I as a real positive function defined in domain $\Omega \subset R^2$. The object and background regions are defined as Ω_i and Ω_e, $\Omega_i \cup \Omega_e = \Omega$, $\Omega_i \cap \Omega_e = \emptyset$. Let $\phi : \Omega \to R$ be an auxiliary function, then Ω_i and Ω_e are represented as the sets $\{(x,y)|\phi(x,y) > 0, (x,y) \in \Omega\}$ and $\{(x,y)|\phi(x,y) < 0, (x,y) \in \Omega\}$, respectively. The boundaries between different regions are defined as the zero level set of ϕ implicitly.

Given the level set function, ϕ, the basic form of the energy function of the proposed method is as

$$E(\phi) = \alpha \cdot E_R(\phi) + \beta \cdot E_C(\phi) + \gamma \cdot E_P(\phi) \tag{1}$$

where $E_R(\phi)$ is the data component for modeling the image information of different regions; $E_C(\phi)$ is the regularization component for controlling the length of the boundaries and preventing over-segmentation; and $E_P(\phi)$ is a term for controlling

the evolution of ϕ. The pre-defined constants α, β and γ are the weights.

2.2. Probability density difference-based active contour model

As mentioned before, the data component, $E_R(\phi)$, is formulated based on the probability density difference. Suppose that the probability densities of intensities in different regions have some prior forms (e.g., Gaussian distribution), and the probability densities can be computed by probability estimation methods (e.g., maximum likelihood, EM, supervised learning, etc.). Defining the estimated probability densities of the intensities in Ω_i and Ω_e as p_i^E and p_e^E, then the actual probability densities of the intensities in Ω_i and Ω_e are p_i and p_e, respectively. The difference between the actual and estimated probability densities is measured by

$$D(p, p^E) = \sum_{i=0}^{255} p(i)(p(i) - p^E(i))^2 \tag{2}$$

The purpose of the segmentation is to partition the image into object and background regions. With such partition, the total weighted difference between the corresponding actual and estimated intensity probability distributions of the regions can be minimized. This criterion can be formulated as the following data component:

$$E_R(\phi) = r_i \cdot A_i \cdot D(p_i(\phi), p_i^E(\phi)) + r_e \cdot A_e \cdot D(p_e(\phi), p_e^E(\phi)) \tag{3}$$

where r_i and r_e are two pre-determined real positive numbers; and A_i and A_e are the areas of Ω_i and Ω_e, respectively:

$$A_i = \int \int_{\Omega_i} dx\,dy, \quad A_e = \int \int_{\Omega_e} dx\,dy$$

This criterion is based on the following two ideas. (1) When $E_R(\phi)$ is minimized, the differences between the actual and estimated probability densities of corresponding partitioned regions are minimum. This property makes the corresponding actual and estimated probability densities be in correspondence to each other. (2) If the estimated probability densities can model the probability densities of the real regions suitably, the model can segment the image effectively. This is because of the fact that the corresponding actual and estimated probability densities are close to each other when $E_R(\phi)$ is minimized. If the estimated probability densities are well modeled, the actual probability densities can be well handled, and a successful segmentation is achieved.

The weights of the probability differences in different regions are determined by two aspects. The first one is the pre-determined weights (r_i and r_e). These two weights can be seen as the pre-defined importance of different regions. If the probability difference of the object (background) region needs to be considered more importantly, the corresponding weight, $r_i(r_e)$, should be higher than another weight [35]. The second one is the areas of object and background regions. It is based on the following idea. If one region is emphasized by the weights, when $E_R(\phi)$ is minimized, the corresponding actual and estimated probability densities are closer to each other. With this property, the emphasized region is handled more suitably. By utilizing the areas as weights, the larger region is emphasized, and more pixels are handled better. Without area weights, different regions are treated equally, this may over-emphasize the smaller regions, and the pixels in the larger regions may not be considered well.

In the proposed method, the actual probability densities can be calculated directly:

$$p_i(g) = \frac{\int \int_{\Omega_i} \delta(I_{x,y} - g)\,dx\,dy}{A_i}, \quad g \in [0, 255] \tag{4}$$

$$p_e(g) = \frac{\int\int_{\Omega_e} \delta(I_{x,y}-g)\,dx\,dy}{A_e}, \quad g \in [0,255] \tag{5}$$

where $\delta(\cdot)$ is the Dirac function, g is the intensity level and $I_{x,y}$ is the intensity of pixel (x,y).

The calculation of estimated probability densities is critical. Ref. [24] proposed that, with the influence of speckle noise, the intensities of different regions can be modeled as Rayleigh distribution with different parameter σ^2:

$$p(I,\sigma^2) = \left(\frac{I}{\sigma^2}\right) \cdot \exp\left(-\frac{I^2}{2\sigma^2}\right) \tag{6}$$

and some existing approaches [20,38] utilized this prior for US image segmentation. In this paper, shifted Rayleigh distribution is utilized for modeling the probability densities:

$$p(I,a,b) = \begin{cases} \dfrac{2}{b}(I-a) \cdot \exp\left(-\dfrac{(I-a)^2}{b}\right), & I \geq a \\ 0, & I < a \end{cases} \tag{7}$$

where a and b are the parameters to be determined. Since the computation complexity is very high if using EM method for estimation, an approximate method is employed in this paper.

For a shifted Rayleigh distribution function, there are the following relationships [39]:

$$\mu_p = a_p + \sqrt{\pi b_p/4} \tag{8}$$

$$\sigma_p^2 = \frac{b_p(4-\pi)}{4} \tag{9}$$

where μ_p and σ_p^2 are the mean and variance, respectively. The parameters of the estimated probability densities of different regions are determined as $\hat{a}_j$ and $\hat{b}_j$, $j \in \{i,e\}$:

$$\hat{a}_j = \mu_j - \sqrt{\pi\hat{b}_j/4}, \quad j \in \{i,e\} \tag{10}$$

$$\hat{b}_j = \frac{4\sigma_j^2}{4-\pi}, \quad j \in \{i,e\} \tag{11}$$

where μ_i, μ_e, σ_i^2 and σ_e^2 are the means and variances of Ω_i and Ω_e, respectively.

Introducing the heaviside function $H(\cdot)$ and level set function ϕ into Eqs. (2) and (3), the data component $E_R(\phi)$ can be re-written as

$$E_R(\phi) = \sum_{j \in \{i,e\}} \int\int_{\Omega} r_j(p_j(I_{x,y})-p_j^E(I_{x,y}))^2 M_j(\phi_{x,y})\,dx\,dy, \quad M_j(\phi_{x,y})$$
$$= \begin{cases} H(\phi_{x,y}), & j=i \\ 1-H(\phi_{x,y}), & j=e \end{cases} \tag{12}$$

2.3. Preventing over-segmentation and regularizing evolution of level set function

For handling noise and preventing over-segmentation, the length of boundary curves is introduced into the energy function [37]:

$$E_C(\phi) = \int\int_{\Omega} |\nabla H(\phi_{x,y})|\,dx\,dy \tag{13}$$

For regularizing the evolution of the level set function, a non-re-initialization approach is adopted, and a punishing component is utilized [40]:

$$E_P(\phi) = \int\int_{\Omega} \frac{1}{2}(|\nabla\phi|-1)^2\,dx\,dy \tag{14}$$

The punishing component prevents the evolving level set function from being too flat or too steep, and with this component, a larger timestep can be utilized to accelerate the evolution to reach the convergence.

2.4. Minimization of the energy function

Combining Eqs. (12)–(14), the complete energy function is written as

$$E(\phi) = \alpha \cdot \sum_{j \in \{i,e\}} \int\int_{\Omega} r_j(p_j(I_{x,y})-p_j^E(I_{x,y}))^2 M_j(\phi_{x,y})\,dx\,dy$$
$$+ \beta \cdot \int\int_{\Omega} |\nabla H(\phi_{x,y})|\,dx\,dy + \gamma \cdot \int\int_{\Omega} \frac{1}{2}(|\nabla\phi_{x,y}|-1)^2\,dx\,dy \tag{15}$$

With total variation method, the associated gradient flow is derived:

$$\begin{cases} \dfrac{\partial\phi}{\partial t} = \delta(\phi)\left[-\alpha \cdot r_i \cdot (p_i-p_i^E)^2 + \alpha \cdot r_e \cdot (p_e-p_e^E)^2 + \beta\,\mathrm{div}\left(\dfrac{\nabla\phi}{|\nabla\phi|}\right)\right] \\ \quad + \gamma \cdot \left(\Delta\phi - \mathrm{div}\left(\dfrac{\nabla\phi}{|\nabla\phi|}\right)\right) \quad \text{in } [0,\infty) \times \Omega \\ \phi(x,y,0) = \phi^0(x,y) \quad \text{in } \Omega \\ \dfrac{\delta(\phi)}{|\nabla\phi|} \cdot \dfrac{\partial\phi}{\partial\vec{n}} = 0 \quad \text{on } \partial\Omega \end{cases} \tag{16}$$

where ϕ^0 is the initial condition, and the last equation in Eq. (16) is the boundary condition. Since the proposed method can model US image well and is not sensitive to the initial condition, the initial condition can be easily formulated as

$$\phi_{x,y}^0 = \begin{cases} -c_0, & (x,y) \in \Omega_0-\partial\Omega_0 \\ 0, & (x,y) \in \partial\Omega_0 \\ c_0, & (x,y) \in \Omega-\Omega_0 \end{cases} \tag{17}$$

where c_0 is a pre-determined constant, and $\partial\Omega_0$ is the initial boundary curve and formulated as the following pixel set (M and N are the width and height of the image, respectively):

$$\partial\Omega_0 = \{(x,y)|(x,y) \in \Omega, \ (M/4 \leq x \leq 3M/4, y=N/4) \text{ or}$$
$$(M/4 \leq x \leq 3M/4, y=3N/4) \text{ or}$$
$$(x=M/4, N/4 \leq y \leq 3N/4) \text{ or } (x=3M/4, N/4 \leq y \leq 3N/4)\} \tag{18}$$

For performing numerical calculation, the Delac function, $\delta(\cdot)$, is approximated [34]:

$$\delta_\varepsilon(z) = \frac{1}{\pi} \cdot \frac{\varepsilon}{\varepsilon^2+z^2} \tag{19}$$

The parameter $\varepsilon = 1.0$ was used in the experiments.

The gradient flow in Eq. (16) is discretized by the central difference, and the complete approximation is

$$\frac{\phi_{i,j}^{n+1}-\phi_{i,j}^n}{\Delta t} = \delta_\varepsilon(\phi)[-r_i \cdot \alpha(p_i-p_i^E)^2 + r_e \cdot \alpha(p_e-p_e^E)^2 + \beta \cdot K_{i,j}] + \gamma \cdot (L_{i,j}-K_{i,j}) \tag{20}$$

$$K_{i,j} = \mathrm{div}\left(\frac{\nabla\phi}{|\nabla\phi|}\right) = D_{i,j}^{0x}\left(\frac{D_{i,j}^{0x}\phi}{\sqrt{(D_{i,j}^{0x}\phi)^2+(D_{i,j}^{0y}\phi)^2}}\right) + D_{i,j}^{0y}\left(\frac{D_{i,j}^{0y}\phi}{\sqrt{(D_{i,j}^{0x}\phi)^2+(D_{i,j}^{0y}\phi)^2}}\right) \tag{21}$$

$$L_{i,j} = \Delta\phi = D_{i,j}^{0xx}\phi + D_{i,j}^{0yy}\phi \tag{22}$$

where D^0 is the central difference operator.

The steps of the proposed segmentation method are summarized as follows:

(a) Initialize the level set function ϕ by ϕ^0.
(b) Compute the actual and estimated probability densities of the object and background regions using Eqs. (4), (5), (10) and (11).
(c) Use Eqs. (20)–(22) to compute ϕ^{n+1} from ϕ^n.
(d) Check the convergence of ϕ, if it does not reach the steady state or the maximum number of iterations, go to step b.

3. Experimental results

3.1. Segmentation of synthetic images

For studying the characteristics of the probability density difference based-model, the proposed method was applied to a series of synthetic images first. The synthetic images are corrupted by two kinds of Rayleigh noises ("spatially uncorrelated" and "spatially correlated" noises) with different levels. The intensities of different regions in the synthetic images can be considered as shifted Rayleigh-distribution with different parameters, and the estimated probability densities will be well modeled. Therefore, the proposed method can segment the corresponding images well. The "spatially uncorrelated" noise was produced by generating complex white Gaussian noise at different levels and taking the magnitudes of the random fields [24]. And the "spatially correlated" noise was produced by using low-pass complex white Gaussian noise at different levels, and taking the magnitudes of the filtering output [41]. According to [42], a 3×3 averaging filter is utilized as the low-pass filter for generating "spatially correlated" noise. The levels of the noise are denoted by signal-noise ratio (SNR). In this paper, the SNR of a synthetic image is defined as the following (the unit is dB):

$$SNR(I_n) = 10 \log_{10} \frac{\sum_{(x,y) \in \Omega}(I_o(x,y) - mean(I_o))^2}{\sum_{(x,y) \in \Omega}(I_n(x,y) - I_o(x,y))^2}$$

where I_o and I_n are the noise-free and noise-corrupted images, respectively; and $mean(\cdot)$ is the mean of the intensities. In the experiments, all the noise-corrupted images are generated from the same noise-free image as shown in Fig. 1(a), and the corresponding positions of object and background regions of the image are shown in Fig. 1(b). As a logarithm, the SNR of a synthetic image can be either positive or negative. The lower the SNR is, the more serious the noise in the corrupted image is.

According to [40], the weight of punishing term, γ, is inversely proportional to the timestep Δt. The product of γ and Δt is less than 0.25, and the value of Δt is less than 10.0 for archiving a stable solution. The value of Δt was selected as 3.0, and

$\gamma = 0.2/3.0$ was determined by experiments. The parameter c_0 should be larger than 2ε, where ε is the parameter of the approximated Delac function (Eq. (19)) [40]. If c_0 is too large (>10.0), the level set function becomes too steep at the beginning of the evolution and it may slow down the convergence. Based on above discussion, c_0 was selected as 4.0 in the experiments. The importance of different regions of the synthetic images is considered as the same, i.e., the pre-defined weight parameters are selected equally: $r_i = 1.0$ and $r_e = 1.0$.

The weights of the data component and regularization component, α and β, were selected by experiments. It was discovered that the value of α should be proportional to the image size. It can be written as $A \cdot a$, where A is the image size and a is the weight parameter. The value of a was selected in the range [0.01, 1.0]. It was found that when $a > 0.5$, the evolving level set function may change dramatically in each iteration and the segmentation process may become unstable, i.e., the evolution may fall into an unsuitable local minimum. However, if a is too small, it takes too many iterations to reach convergence. Finally, a is selected as 0.1 based on experiments. The relationship between utilizing image information and preventing over-segmentation can be written as the ratio $r_{dc} = a/\beta$. The ratio r_{dc} should be selected carefully. If r_{dc} is too high, the image information is over-emphasized and the length of the boundaries is not considered well. In this situation, too many trivial regions (over-segmentation) may be obtained. On the other hand, if r_{dc} is too low, the length of the boundaries is over-controlled, and the image information will not be focused. This causes the evolution to converge in an unsuitable position. The value of β was selected in the range [0.5, 10.0]. Because the segmentation of synthetic images aims at finding the characteristics of the data component, the data component should play a major role, and the weight β is selected as 1.5 which is quite low. Although the weight of the regularization component is low, the proposed method can adapt to the noise at different levels since the data component is well modeled.

The proposed method is applied to 14 "spatially uncorrelated" synthetic images whose signal/noise ratios (SNR) are from -13.25 to -0.95 dB (as listed in Table 1). The lower the SNR is, the more serious the noise is. For comparison, geodesic active contour (GAC) model [33,43] and active contour without edges (ACWE) model [34] are also applied to the same images. The GAC is an "edge-driven" model which utilizes edge indicators to detect the boundaries between different regions. The ACWE model is a "region-driven" model which utilizes the means of different regions for modeling the image and accomplishing the

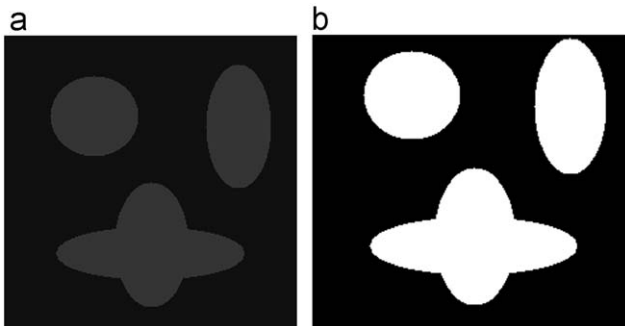**Fig. 1.** (a) The original noise free image; and (b) the grand truth of the pre-defined regions (the object regions are marked by white color).

Table 1
The RSEs of the segmentation results of the "spatially uncorrelated" synthetic images.

SNR (dB)	RSE		
	GAC model (%)	ACWE model (%)	The proposed method (%)
−0.95	0.53	0.03	0.02
−1.73	0.52	0.02	0.02
−2.98	0.51	0.06	0.06
−3.95	0.51	0.14	0.13
−5.71	0.51	0.20	0.20
−6.97	0.94	0.34	0.25
−7.92	1.10	0.45	0.35
−8.69	1.19	0.60	0.49
−9.98	1.28	1.08	0.53
−10.50	1.43	1.30	0.74
−11.36	1.53	1.90	0.81
−11.75	1.47	2.28	0.78
−12.68	1.95	3.56	1.19
−13.25	2.30	4.12	1.23

segmentation task. It has been justified that both of the above two approaches can produce good segmentation results for many kinds of images. A sample of the segmentation of "spatially uncorrelated" synthetic images is shown in Fig. 2. Fig. 2(a) is the noise-corrupted image ($SNR = -13.25$ dB), and the white contours mark the pre-defined boundary curves between object and background regions. Comparing the results obtained by the GAC model (Fig. 2(b)), the ACWE model (Fig. 2(c)) and the proposed method (Fig. 2(d)), the proposed method is the most successful. The GAC model detects the boundaries utilizing edge indicators. When there is serious noise, the edge indicators are affected, and the GAC model may converge at an unsuitable local minimum. There are some unsuitable trivial regions in the objects and background generated by the ACWE model. This is due to the fact that the ACWE model only utilizes the means of different regions, and it is not good enough to model the image. In the proposed method, the estimated probability density can effectively model different regions. By minimizing the probability difference, the actual probability densities in the partitioned regions are close to the corresponding estimated probability densities. The actual and estimated probability densities of the object and background regions generated by the proposed method are shown in Figs. 2(e) and (f), respectively. It shows that when the evolution converges, the actual and estimated probability densities are very close to each other in both object and background regions, i.e., a successful segmentation is obtained.

Since the accurate positions of object and background regions of the synthetic images are precisely known in advance, it is rational to use the ratio of segmentation error (RSE) for evaluating the performance. If the total number of the pixels in a synthetic image is N_T, and the number of the pixels mistakenly classified is N_{SE}, then RSE can be calculated as

$$RSE = N_{SE}/N_T$$

Lower RSE means that there are fewer pixels misclassified, i.e., the image can be segmented more accurately. The segmentation results are listed in Table 1. It shows that, when the SNR is high (e.g., $SNR > -6.97$ dB), the differences between the above three methods are small. However, when SNR is lower, due to unsuitable modeling, the GAC and ACWE cannot be adaptive to the noise and their RSEs increase drastically. Because of the well modeled data component, the proposed method obtains much better results. For all images, the RSEs obtained by the proposed method are quite low, i.e., the proposed method can be adaptive to different levels of noise and the segmentation results are good.

There are 20 "spatially correlated" synthetic images in the experiments, and their SNRs are from -14.43 to -1.40 dB (as listed in Table 2). In these images, the noise is spatially correlated. In this situation, the consideration of the relationship among neighboring pixels is not effective for handling noise. Hence, the modeling becomes more important. If the data component is not well modeled, it is affected by the noise and poor segmentations may be produced, since the regularization component cannot be very helpful in this situation. Due to this fact, the segmentation of "spatially correlated" images is more difficult than the segmentation of "spatially uncorrelated" images. A sample of
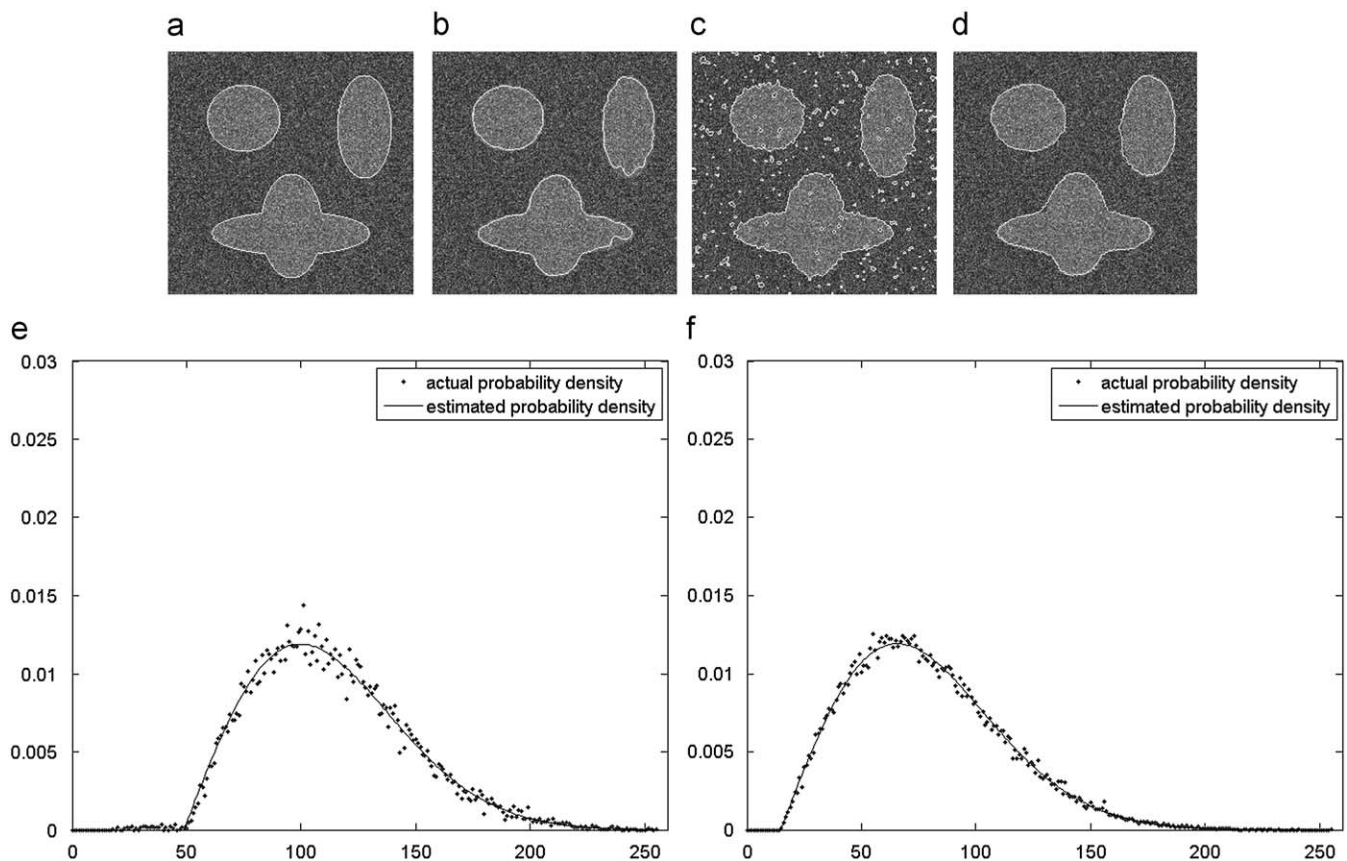

Fig. 2. The segmentation of a "spatially uncorrelated" synthetic image ($SNR = -13.25$ dB): (a) the original image (the white contour marks positions of the pre-defined boundaries); (b) the result produced by the GAC model; (c) the result produced by the ACWE model; (d) the results produced by the proposed method; (e) the actual and estimated probability densities of the intensities in the object region generated by the proposed method; and (f) the actual and estimated probability densities of the intensities in the background region generated by the proposed method

the segmentation of "spatially correlated" synthetic images is shown in Fig. 3 (SNR= − 14.43 dB). The noise corrupted image and the pre-defined boundary curve are shown in Fig. 3(a). With serious noise, there are many trivial regions having similar intensities, and the boundaries between object and background

Table 2
The RSEs of the segmentation results of the "spatially correlated" synthetic images.

SNR (dB)	RSE		
	GAC model (%)	ACWE model (%)	The proposed method (%)
− 1.40	1.06	0.06	0.06
− 4.48	1.76	0.20	0.19
− 6.20	1.78	0.53	0.37
− 7.45	7.68	1.19	0.65
− 8.44	18.50	1.54	0.53
− 9.24	27.92	2.04	0.83
− 9.85	31.64	2.67	0.87
− 10.46	25.21	3.56	1.07
− 11.02	31.36	4.47	1.30
− 11.47	32.88	5.05	1.32
− 11.81	36.34	4.50	1.29
− 12.26	31.44	6.03	1.64
− 12.54	31.94	5.75	1.53
− 12.94	34.39	7.72	1.78
− 13.18	32.20	6.98	1.68
− 13.47	34.78	7.46	1.60
− 13.75	34.96	7.89	1.59
− 14.01	36.74	8.68	1.68
− 14.23	35.90	10.14	1.76
− 14.43	32.79	9.15	1.48

regions are very blurry. The results of GAC model, ACWE model and the proposed method are shown in Figs. 3(b), (c) and (d), respectively. Both GAC model (RSE=32.79%) and ACWE model (RSE=9.15%) cannot produce accurate segmentation results. Since many local regions in the image have similar intensities and the intensities around these local regions vary drastically, the edge indicator of GAC model is seriously affected, and trapped into an unsuitable local minimum. ACWE model utilizes the means of different regions, and the regions with similar intensities are not handled well, therefore, many trivial regions are mistakenly produced. The proposed method can model suitably, therefore, the noise is well handled and the image is successfully segmented (RSE=1.48%). The corresponding actual and estimated probability densities of the object and background regions generated by the proposed method are shown in Figs. 3(e) and (f). It can be seen that, the corresponding actual and estimated probability densities fit each other very well when the evolution converges.

The RSEs of the segmentation results of the "spatially correlated" synthetic images are presented in Table 2. The GAC model cannot treat most of the images well. The "spatially correlated" noise seriously affects the edge indicator; therefore, the GAC model converges in unsuitable local minimums. Some images (e.g., SNR > − 9.24 dB) can be treated well by the ACWE model, however, it cannot segment the seriously corrupted images well. For all the "spatially correlated" synthetic images, the RSEs of the proposed method are very low, i.e., there are very few pixels misclassified. This demonstrates that the proposed method can model the images suitably and effectively, and segment the images accurately.
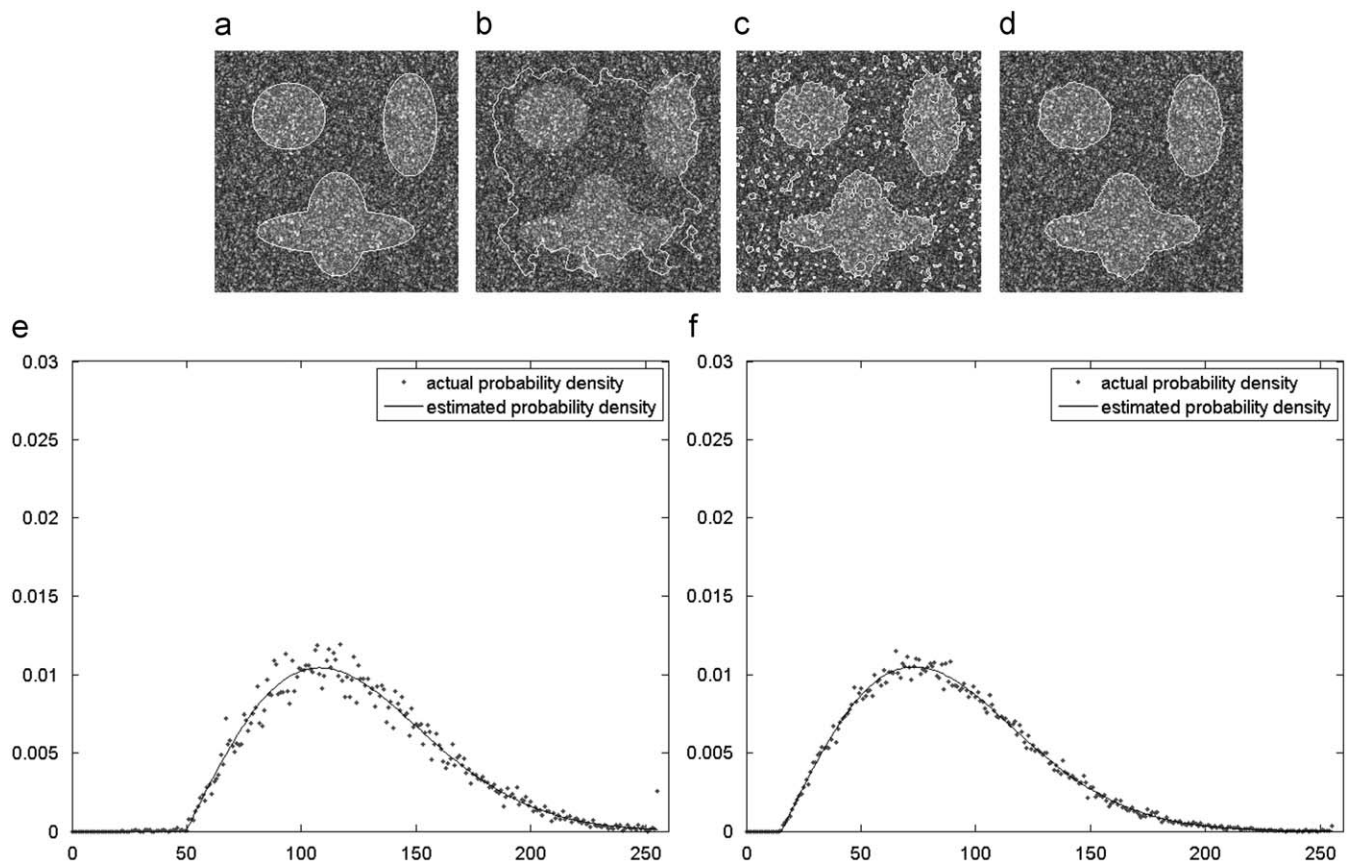

Fig. 3. The segmentation of a "spatially correlated" synthetic image (SNR= − 14.43 dB): (a) the original image (the white contour marks the positions of the pre-defined boundaries); (b) the result produced by the GAC model; (c) the result produced by the ACWE model; (d) the results produced by the proposed method; (e) the actual and estimated probability densities of the intensities in the object region generated by the proposed method; and (f) the actual and estimated probability densities of the intensities in the background region generated by the proposed method.

3.2. Segmentation of BUS images

A database including 79 BUS images (33 benign and 46 malignant) is utilized as the clinical images for evaluating the proposed method. In most of BUS images, due to serious speckle noise, there are blurry boundaries between different regions and the contrast is also low. In addition, the shapes, locations and areas of tumor regions are in great variations [8]. All these factors make the segmentation of BUS images be a very difficult task. The images were obtained from the Second Affiliated Hospital of Harbin Medical University (Harbin, China). The BUS images were collected by using a VIVID 7 (GE, Horten, Norway) with a 5–14 MHz linear probe, and captured directly from the video signals. Informed consent to the protocol was obtained from all patients in the study.

Usually manual delineations produced by experienced radiologists were utilized for evaluating segmentation methods [8,14]. Since there are inter-observer variations between delineations of different radiologists, the averaged delineations by multiple radiologists are employed for evaluating segmentation methods [44]. According to [44,45], in this paper, two experienced radiologists delineated the breast tumor regions manually, and the corresponding delineations are averaged for the evaluation. In addition, statistical approach is also utilized for the evaluation [44].

Here, the weight β is set to 4.0 which is larger than that for the synthetic images, since the SNR and contrast are often low and the boundaries between different tissue regions of the BUS images are very blurry. Larger β is needed to prevent over-segmentation. Different β values are tested, considering both the image information and preventing over-segmentation, the weight β is selected as 4.0 finally.

In this paper, three other well-studied approaches: GAC model, ACWE model and a specialized BUS image segmentation method [31] were also applied to the same BUS images for comparison. The segmentation method in [31] is a hybrid approach having three steps. (1) The speckle noise is suppressed by anisotropic diffusion filter [46] and stick filter [47]. (2) The noise suppressed image is binarized by thresholding [48], and the noise suppressed image and thresholded image are combined to generate a pre-processed image. (3) An "edge-based" level set method is utilized for accomplishing the segmentation task. In the experiments, the configuration of the initial condition of the level set method employed in this approach is carefully considered. Since the "edge-based" level set method may be sensitive to the noise and initial condition, and easy to converge on an unsuitable local minimum, the result of the thresholded BUS image is utilized as the initial condition [19]. According to [19], with thresholding, the initial condition may be very close to the real boundaries of the tumor regions, and this can help the segmentation method to avoid converging in unsuitable local minimum and to accelerate the processing speed.

The original image with two independent manual delineations of the breast tumor region is shown in Fig. 4(a), and the averaged manual delineation is shown in Fig. 4(b). The tumor regions generated by the GAC model, the ACWE model and the approach in [31] are shown in Figs. 4(c), (d) and (e), respectively. Compared to Fig. 4(b), it shows that the tumor region generated by the GAC model cannot cover the whole tumor region. This is due to the serious speckle noise, there are many local minimums, and the GAC model converges on an unsuitable local minimum. The tumor region generated by the ACWE model is also inaccurate and many normal tissues are mistakenly covered. Since only the means of different regions are employed, it is not able to model the BUS images well.

The tumor region generated by the approach in [31] also covers many normal tissue regions (Fig. 4(e)). This is due to two reasons. The first one is the failure of its pre-processing. The result of the pre-processing is shown in Fig. 4(f) (white contours denote the result of thresholding). The noise is suppressed and the contrast of the image is enhanced, however, there are some regions mistakenly partitioned by thresholding. It is harmful to further operation and not easy to separate the real tumor and normal tissue regions. Another one is that the employed level set method only uses the edge information, and it is not enough to handle the pre-processed image well. In the pre-processed image, the edge response is very strong at the boundaries between the regions generated by thresholding. For this situation, the level set method only converges at this kind of positions, and it fails in finding the real tumor boundary.

The segmentation by the proposed method is shown in Fig. 4(g), and the generated tumor region is shown in Fig. 4(h). Comparing to Fig. 4(b), it shows that the generated tumor region is much closer to the averaged manual delineation. The actual and estimated probability densities of the object and background regions generated by the proposed method are shown in Figs. 4(i) and (j), respectively. The actual and estimated probability densities are in good correspondence with each other in both object and background regions. This shows that by employing the shifted-Rayleigh distribution and the estimation method, both the hyper- and hypo-echoic regions in the BUS images are effectively modeled, and successful segmentation is achieved.

Fig. 5(a) shows that the boundary between the tumor region and normal tissue region is blurry and the contrast of the image is quite low. The GAC model (Fig. 5(b)) cannot handle the blurry boundary well, and it did not converge on the real boundary of the tumor region. The ACWE model (Fig. 5(c)) and the approach in [31] (Fig. 5(d)) also did not generate accurate tumor regions. However, the proposed method (Fig. 5(e)) can handle the blurry boundaries very well, and the generated tumor region is very close to the averaged manual delineation.

In this paper, several approaches and metrics are utilized for evaluating the segmentation results of the clinical images. Three overlapping area error metrics [49]: the true positive ratio (TP), the false positive ratio (FP) and the similarity (SI) were utilized. Let A_a be the pixel set of the tumor region selected by the proposed method and A_m be the pixel set of the corresponding real tumor region, the three error metrics are

$$TP = \frac{|A_m \cap A_a|}{|A_m|}, \quad FP = \frac{|A_m \cup A_a - A_m|}{|A_m|}, \quad SI = \frac{|A_m \cap A_a|}{|A_m \cup A_a|}$$

When the TP ratio is higher, more real tumor regions are covered by the generated tumor regions. When the FP ratio is lower, fewer normal tissue regions are covered by the generated tumor regions. When the SI ratio is higher, the generated tumor region is more similar to the radiologist's delineation, i.e., the overall performance is better. As mentioned before, the averaged manual delineations of the tumor regions are utilized as the grand truth. The overlapping area error metrics of the GAC model, ACWE model, approach in [31] and proposed method are listed in Table 3.

It shows that the TP ratio of the GAC model is low (TP=71.65%). This is due to that some real tumor regions are missed by the GAC model, as shown in Fig. 4. The TP ratios of the other three methods are all higher than 90%, i.e., most of real tumor regions can be located by all of the three methods. The TP ratio of the proposed method is a little lower than that of the ACWE model and the approach in [31]. This is due to that, for many cases, the regions around the boundaries are very blurry, and in these regions, the real boundaries are difficult to discriminate. Such blurry regions are usually included in the manual delineations of the radiolo-
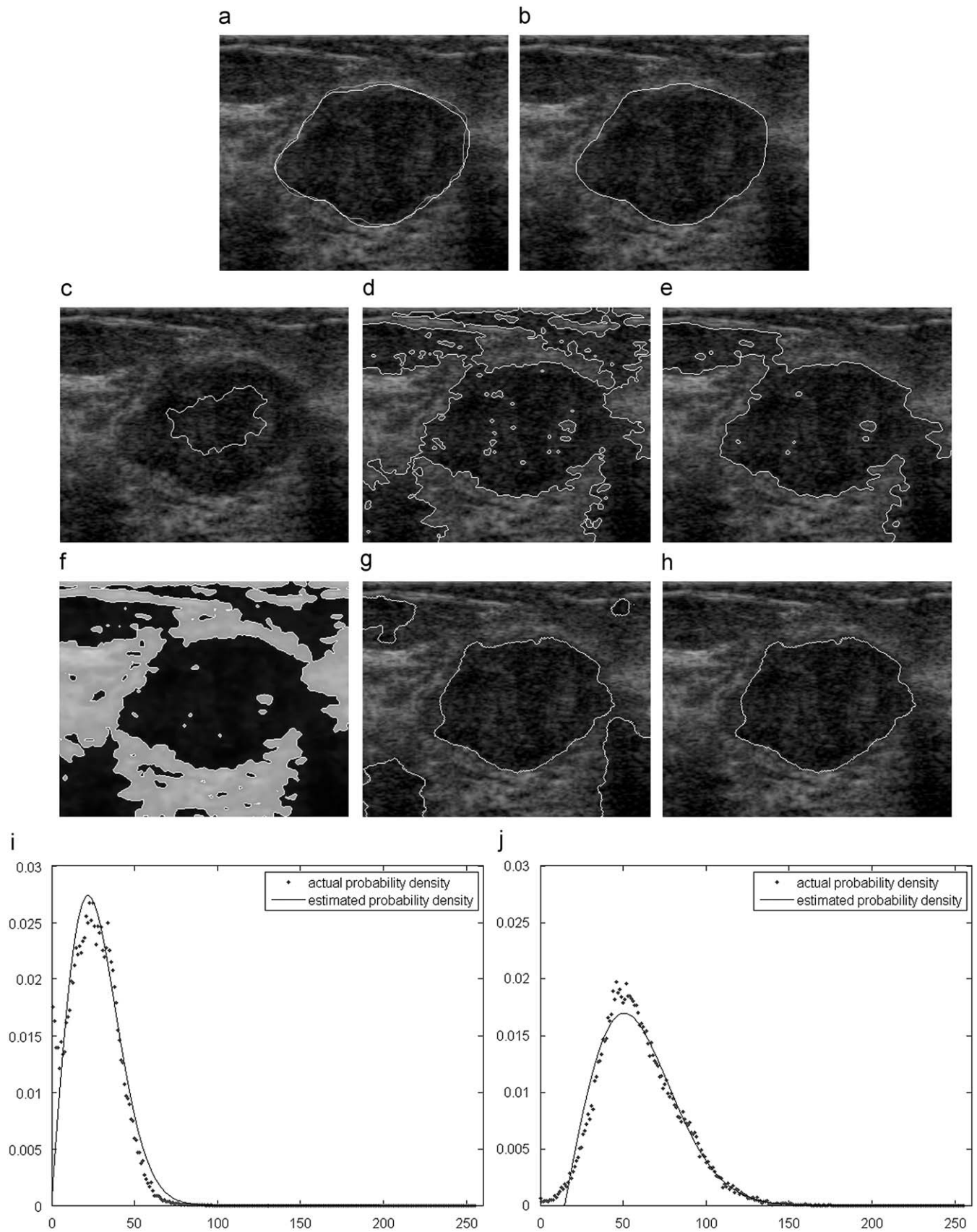
Fig. 4. The segmentation of a BUS image: (a) the original image (the lighter contour marks the manual delineation of the breast tumor region by an experienced radiologist, and the darker contour marks the manual delineation of the breast tumor region by another experienced radiologist); (b) the averaged manual delineation of the breast tumor region marked by the white contour; (c) the tumor region generated by the GAC model; (d) the tumor region generated by the ACWE model; (e) the tumor region generated by the approach in [31]; (f) the preprocessing result of the approach in [31] (white contour marks the result of thresholding); (g) the segmentation result when the proposed method converges; (h) the tumor region generated by the proposed method; (i) the actual and estimated probability densities of the intensities in the object region generated by the proposed method; and (j) the actual and estimated probability densities of the intensities in the background region generated by the proposed method.
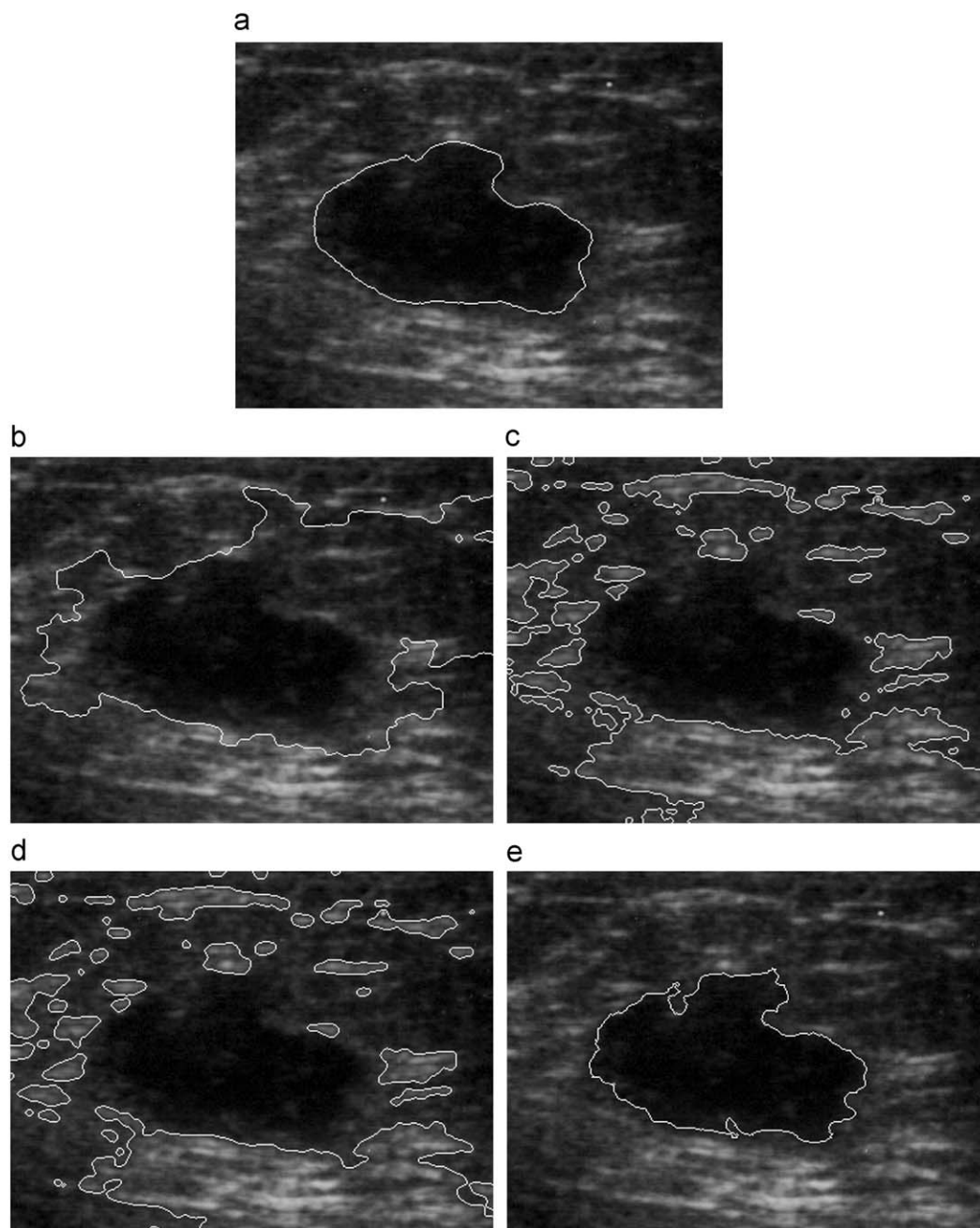
Fig. 5. The segmentation of another BUS image having low contrast and blurry boundaries: (a) the original image (the white contour marks the averaged manual delineation of the breast tumor region); (b) the tumor region generated by the GAC model; (c) the tumor region generated by the ACWE model; (d) the tumor region generated by the approach in [31]; and (e) the tumor region generated by the proposed method.

Table 3
Overlapping area error metrics of the segmentation of clinical BUS images.

Method	TP ratio (%)	FP ratio (%)	Similarity (%)
GAC model	71.65	12.31	64.41
ACWE model	96.26	52.17	73.56
The approach in [31]	95.76	60.33	69.61
The proposed method	93.93	6.98	88.07

gists. However, with suitable modeling, the proposed method can handle the blurry regions well and find the real boundaries. Therefore, some regions covered by the averaged manual

delineations are not in the tumor regions generated by the proposed method, and this makes the TP ratio lower. For the ACWE model and the approach in [31], some normal tissues are mistakenly contained in the generated tumor regions, including the blurry surrounding regions, and the TP ratios are higher. However, their segmentations are not accurate, and the higher FP ratios demonstrate this.

The FP ratios of the ACWE model and the approach in [31] are very high (52.17% and 60.33%, respectively). Like the cases in Figs. 4 and 5, although nearly the entire real tumor regions are covered, many unsuitable regions are also included in the tumor regions generated by the ACWE model and the approach in [31]. In addition, these unsuitable regions cannot be separated from the

real tumor regions easily. For CAD systems, this may seriously affect the feature extraction. The *FP* ratio of the GAC model is also quite high (12.31%). For most cases, the GAC model only converges on the inner areas of the real tumor regions as shown in Fig. 4. In some cases, the GAC model cannot handle the blurry boundaries either and unsuitable normal tissue regions are covered, as shown in Fig. 5. The proposed method obtains a much lower *FP* ratio (6.98%). In the tumor regions generated by the proposed method, there are fewer normal tissue regions included and the segmentation is more accurate.

The proposed method obtained the best similarity (88.07%), much higher than that of the GAC model (64.41%), the ACWE model (73.56%) and the approach in [31] (69.61%), i.e., the overall performance of the proposed method is the best.

The second approach for evaluating the performance of the segmentation is the statistical evaluation [44]. In the statistical evaluation, the generated tumor regions are compared to the manual delineations produced by the radiologists, and the manual delineations produced by different radiologists are also compared to each other. In this paper, Williams Index (*WI*) [44,50] is utilized for statistical evaluation. The Williams Index can be calculated as

$$WI = \frac{\frac{1}{2}\sum_{j=1}^{2} P_{0,j}}{P_{1,2}}$$

where $P_{0,j}$ is the mean disagreement between the generated tumor regions and the manual delineations produced by the *j*th radiologist, and $P_{1,2}$ is the mean disagreement between the manual delineations produced by the first and second radiologists. The mean disagreement is defined as

$$P_{j,j'} = \frac{1}{\frac{1}{N}\sum_{i=1}^{N} c(\mathbf{x}_{ij}, \mathbf{x}_{ij'})}, \quad j=0,1,2 \text{ and } j'=0,1,2$$

where N is the number of the BUS cases; $\mathbf{x}_{ij}$ and $\mathbf{x}_{ij'}$ are the tumor regions of the *i*th case produced by the observers j and j', respectively $(j=0(j'=0)$ represents the segmentation method, and $j=1,2(j'=1,2)$ represents the radiologists); $c(\cdot,\cdot)$ is the specific metric for evaluating the difference between the tumor regions produced by different observers. The higher the Williams Index a segmentation method obtains, the more reliable the generated tumor regions are.

$c(\cdot,\cdot)$ is a metric and meets the following three conditions [44]:

(1) $c(A,A) = 0$ and $c(A,B) \geq 0$.
(2) $c(A,B) = c(B,A)$.
(3) $c(A,C) \leq c(A,B) + c(B,C)$.

There are various metrics. In this paper, two kinds of metrics are employed. The Hausdorff distance is employed first. Define two boundary pixel sets of the tumor regions of a BUS case generated by two observers as $B_A = \{a_1, a_2, \ldots, a_m\}$ and $B_B = (b_1, b_2, \ldots, b_n)$, where a_i $(i=1,\ldots,m)$ and b_j $(j=1,\ldots,n)$ are the coordinates of the pixels in sets B_A and B_B. The Hausdorff distance is defined as

$$c_1(B_A, B_B) = \max\{\max_i(d_1(a_i, B_B)), \max_j\{d_1(b_j, B_A)\}\},$$

$$d_1(a_i, B_B) = \min_j \|a_i - b_j\|, \quad d_1(b_j, B_A) = \min_i \|a_i - b_j\|$$

where $\|a_i - b_j\|$ is the Euclidean distance between pixels a_i and b_j.

Another one is the normalized overlapping difference. Define two pixel sets of the tumor regions of a BUS case generated by two observers as R_A and R_B, and the pixel set of the real tumor region of the same image is defined as R_T. The normalized overlapping difference is as following:

$$c_2(R_A, R_B) = \frac{|R_A - R_B| + |R_B - R_A|}{|R_T|}$$

where $|\cdot|$ is the number of the pixels in the corresponding pixel set. Here, the averaged manual delineation is also utilized as R_T for the normalization.

For each method, the Hausdorff distance (mean and standard deviation (*Std*)) between the segmentation results and the manual delineations produced by the two radiologists and the averaged manual delineations, and the corresponding Williams Indices are presented in Table 4. The Hausdorff distance between the manual delineations produced by different radiologists is necessary for calculating the Williams Indices. The mean and *Std* of the Hausdorff distance between the manual delineations produced by the two radiologists are calculated, and *Mean*=22.48 and *Std*=14.41, respectively.

In each column of Table 4, the mean of the Hausdorff distance between the result of the proposed method and the radiologists' manual delineations is the lowest which indicates that the proposed approach is more accurate than other approaches. We would like to indicate that due to inter-observer variations, the segmentation results may be in favor of the manual delineations produced by a specific radiologist. For instance, the smallest mean of the Hausdorff distance is obtained between the result of the proposed method and the manual delineations of radiologist #1. However, the corresponding means of the Hausdorff distances between the results of the proposed approach and the manual delineations of radiologist #2 and the averaged manual delineations are still much lower than that of the other three approaches. This demonstrates that the proposed method is the most accurate comparing with the other approaches in the study. For reducing the inter-observer variations, we used the averaged manual delineations in the experiments.

The proposed method achieves the highest *WI* (0.8656), hence, its segmentation result is the most reliable.

The standard deviations of Hausdorff distances are also computed. In each column, the standard deviation of the Hausdorff distance obtained by the proposed method is the

Table 4
Statistical evaluation with Hausdorff distance.

Method	Hausdorff distance between the results of the method and radiologist #1	Hausdorff distance between the results of the method and radiologist #2	Hausdorff distance between the results of the method and the averaged manual delineation	WI
GAC model	Mean=53.47 Std=25.77	Mean=53.24 Std=24.91	Mean=52.67 Std=24.93	0.4214
ACWE model	Mean=69.56 Std=40.98	Mean=71.58 Std=42.28	Mean=71.71 Std=42.26	0.3187
The approach in [31]	Mean=82.63 Std=41.85	Mean=84.75 Std=42.21	Mean=84.52 Std=42.50	0.2687
The proposed method	Mean=24.19 Std=15.20	Mean=28.04 Std=16.35	Mean=25.07 Std=16.30	0.8656

Table 5
Statistical evaluation with normalized overlapping difference.

Method	Normalized overlapping difference between the results of the method and radiologist #1	Normalized overlapping difference between the results of the method and radiologist #2	Normalized overlapping difference between the results of the method and the averaged manual delineations	WI
GAC model	Mean=0.4156 Std=0.2691	Mean=0.4210 Std=0.2740	Mean=0.4066 Std=0.2710	0.3217
ACWE model	Mean=0.5579 Std=1.0637	Mean=0.5766 Std=1.0666	Mean=0.5591 Std=1.0677	0.2373
The approach in [31]	Mean=0.6439 Std=0.9997	Mean=0.6657 Std=1.0012	Mean=0.6457 Std=1.0034	0.2056
The proposed method	Mean=0.1232 Std=0.0887	Mean=0.1649 Std=0.0680	Mean=0.1305 Std=0.0760	0.9542

Table 6
Correlation of tumor sizes.

Method	Pearson statistic
GAC model	0.7423
ACWE model	0.1705
The approach in [31]	0.1829
The proposed method	0.9241

lowest. This demonstrates that the proposed method has the best reproducibility.

The result of the statistical evaluation with normalized overlapping difference is listed in Table 5. The mean and *Std* of the normalized overlapping difference between the manual delineations produced by the two radiologists are *Mean*=0.1346 and *Std*=0.0586. In the first three columns, it shows that the proposed method obtains much lower means of the normalized overlapping differences than that of the other three approaches. Similar to the case of the Hausdorff distance, the mean of the normalized overlapping difference between the segmentation results produced by the proposed method and the manual delineations produced by radiologist #1 is the lowest. However, for radiologist #2 and the averaged manual delineations, the corresponding means of the normalized overlapping differences are still much lower than that of the other three approaches. This demonstrates that the segmentation of the proposed method is the most accurate. The Williams Index obtained by the proposed method is *WI*=0.9542 which is the highest, i.e., the proposed method is more reliable than the other three methods.

The standard deviations of normalized overlapping differences are also studied. In each column, the standard deviation of normalized overlapping difference obtained by the proposed method is much lower than that of the other three approaches. This also demonstrates that the proposed method is more reproducible.

The correlations between the sizes of the tumor regions generated by the four segmentation approaches and the sizes of the tumor regions determined by the averaged manual delineations are also computed. In this paper, the sizes of breast tumors are defined by the length of the tumor boundary curves [15]. For studying the correlations, Pearson's correlation coefficient [51] is calculated which is defined as

$$r = \frac{\text{cov}(X, Y)}{\sigma_X \sigma_Y}$$

where X and Y are the two sets of tumor sizes obtained by different observers; $\text{cov}(X, Y)$ is the covariance of X and Y; and σ_X and σ_Y are the variances of X and Y, respectively. The higher the correlation coefficient is, the closer the tumor sizes obtained by the two observers are.

The correlation coefficients of the four approaches and the averaged manual delineation are listed in Table 6, respectively. The sizes of the tumor regions generated by the proposed method are the closest to that of the averaged manual delineations.

Although the results obtained by the proposed method are very good, there are still some cases which cannot be handled well by the proposed method. In the first case, some of the real tumor regions cannot be fully covered, as shown in Fig. 6. In the original image (Fig. 6(a)), the boundary of tumor region is very blurry. Manual delineation covers the whole tumor region, including some of the smooth and blurry regions between the tumor and normal tissues. Using the proposed method (Fig. 6(e)), the blurry regions are not well handled. Some of the real tumor regions are missed, and a low *TP* ratio (*TP*=84.20%) is obtained. The *TP* ratio of the GAC model (Fig. 6(b)) is 89.61%, i.e., it covers more tumor regions than that of the proposed method, but some unsuitable regions are also covered by the GAC model and a high *FP* ratio (*FP*=25.86%) is obtained. With lower *FP* ratio (*FP*=9.38%), the proposed method obtains better similarity (*SI*=76.97%) than that of the GAC model (*SI* =71.24%). The segmentation results of the ACWE model (Fig. 6(c)) and the approach in [31] (Fig. 6(d)) are very poor. Although they can cover most of the tumor region, many normal tissues are also mistakenly included. Their *SIs* are only 11.27% and 12.06%, respectively, i.e., much lower than that of the GAC model and the proposed method. Even for this case, the segmentation result of the proposed method is still better than that of other three methods.

The second case is shown in Fig. 7. Most of the tumor region is covered, however, the proposed method could not handle the blurry boundary well, and some surrounding regions are included wrongly (Fig. 7(e)). However, the other three approaches cannot produce good segmentation results either. Using the GAC model, the tumor region is not fully covered (Fig. 7(b)). Using the ACWE model (Fig. 7(c)) and the approach in [31] (Fig. 7(d)), many normal tissues are covered. Even there are some errors, the proposed method can still archive the highest similarity (*SI*=82.00%), much higher than that of the GAC model (*SI*=62.16%), ACWE model (*SI*=33.22%) and the approach in [31] (*SI*=30.94%).

The processing speeds of the four methods are also studied (Table 7). All the four methods were performed on a Core2 PC with 2 GB RAM using MATLAB. Comparing to the GAC and ACWE models, the proposed method needs less time to reach the convergence due to the following two reasons. (1) With suitable modeling, the noise and blurry boundaries can be well handled, and it makes the evolution more efficient. (2) With the non-re-initialization evolution strategy, a larger timestep can be used, and there is no re-initialization processing needed in the evolution of the level set function [40]. The speed of the approach in [31] is faster than that of the proposed method. Since the original image is pre-processed for suppressing noise and enhancing contrast, and the result of the thresholding is
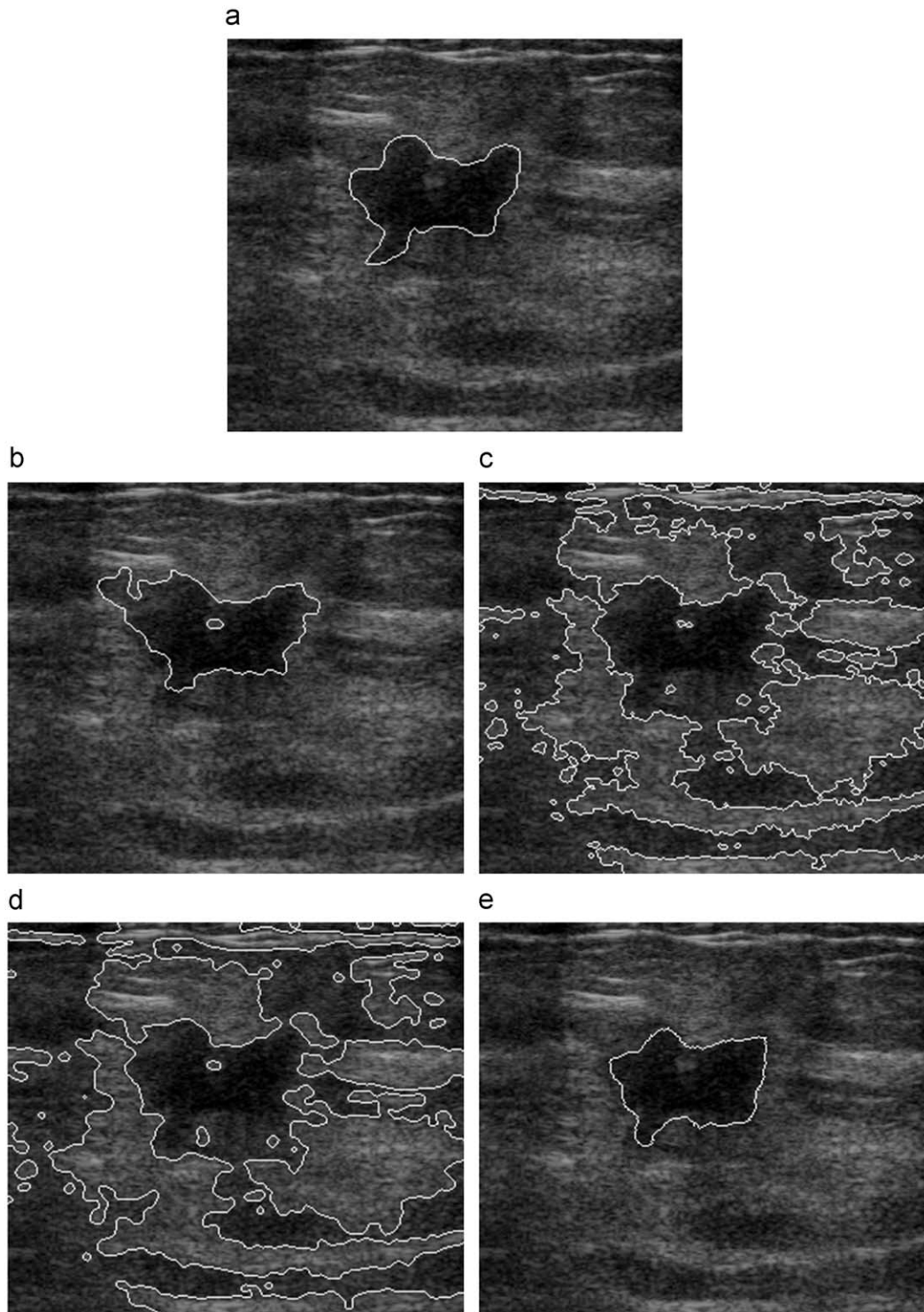
Fig. 6. A sample that the proposed approach cannot fully cover the tumor region; (a) the original image (the white contour marks the averaged manual delineation of the breast tumor region); (b) the tumor region generated by the GAC model; (c) the tumor region generated by the ACWE model; (d) the tumor region generated by the approach in [31]; and (e) the tumor region generated by the proposed method.

utilized as the initial condition, this can accelerate the evolution of the level set function. However, for many cases, segmentation results generated by the approach in [31] are not very accurate. The proposed method utilizes a general initial condition (defined by Eq. (18)) which is usually far away from the boundary of the real tumor region, and it needs longer time to accomplish the segmentation task. However, its segmentation results are more accurate and reliable.

4. Conclusion

In this paper, a novel level set-based active contour approach is proposed for BUS image segmentation. In this method, the energy function is formulated based on the difference between the actual and estimated probability densities of the intensities in different regions. Total variation and finite difference methods are utilized for
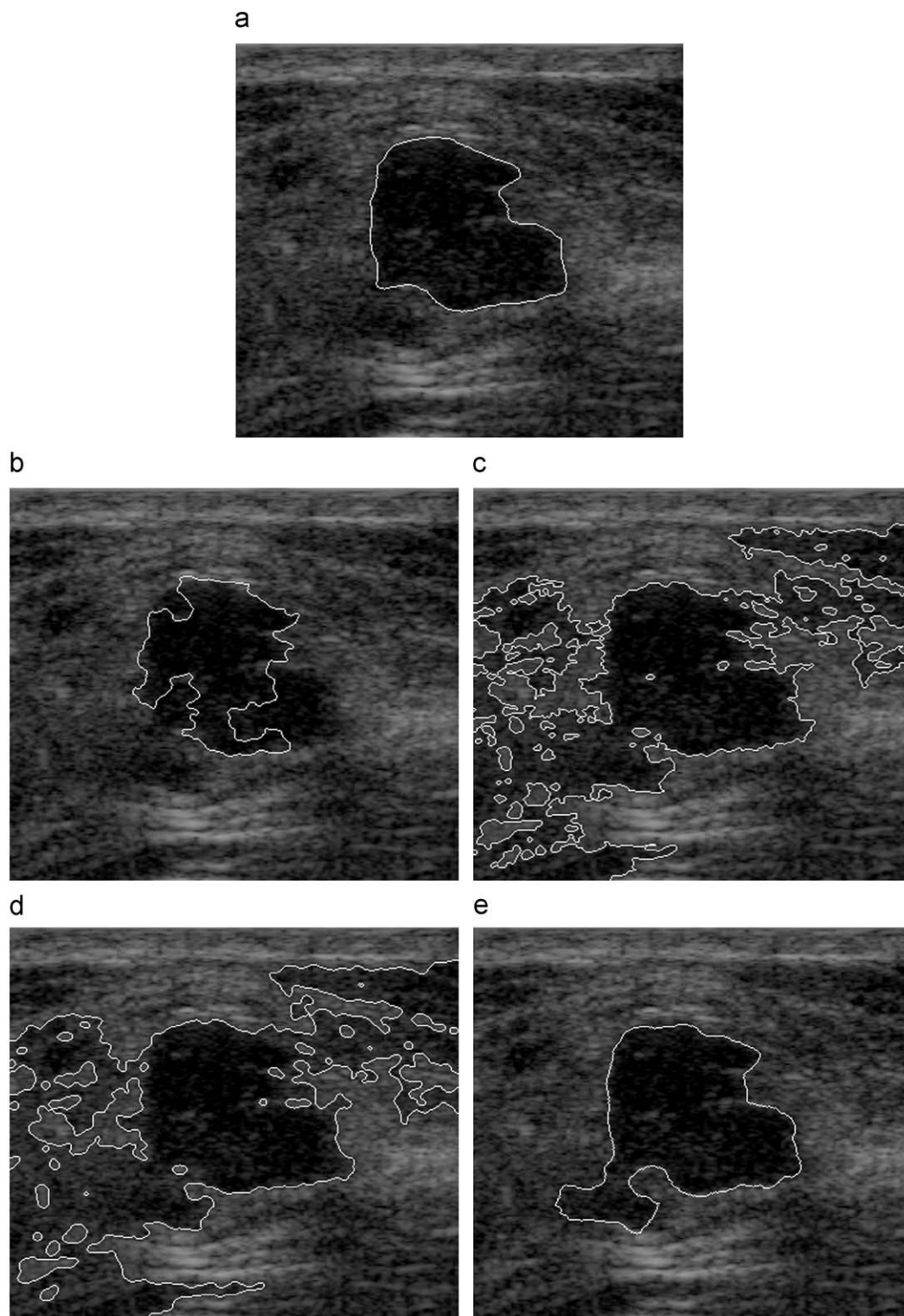
Fig. 7. A sample that the proposed approach covered some normal tissue regions: (a) the original image (the white contour marks the averaged manual delineation of the breast tumor region); (b) the tumor region generated by the GAC model; (c) the tumor region generated by the ACWE model; (d) the tumor region generated by the approach in [31]; and (e) the tumor region generated by the proposed method.

minimizing the energy function to accomplish the segmentation task. For Rayleigh corrupted synthetic images, the experimental results show that the proposed estimation method can produce accurate segmentation if the estimated probability densities are modeled suitably.

The proposed method is also applied to clinical BUS images. For evaluating the performance of the proposed method, the tumor regions generated by the proposed method are compared to the manual delineations of the tumor regions produced by two experienced radiologists. The overlapping area error metrics and

Table 7
Average number of iterations and CPU time to reach convergence.

Method	Average number of iterations	Average CPU time (s)
GAC model	13.5×10^2	184.2
ACWE model	10.4×10^2	171.9
The approach in [31]	2.1×10^2	32.6
The proposed method	3.9×10^2	60.8

statistical evaluations are utilized. Three other methods are also applied to the same images for comparison. The proposed method produces much better results than that of the other three methods. The processing speeds of the proposed method and the other three methods are also studied. The speed of the proposed method is slightly slower than that of the fastest one; however, the accuracy of the proposed method is the highest.

Because of its effectiveness, the proposed method may find wide application in BUS imaging and CAD systems. In the future, three issues should be investigated. (1) There are some cases that the proposed approach cannot handle well. (2) More clinical images should be employed for evaluating and improving the proposed method. (3) Integrate the proposed method into CAD systems for generating better regions of interest (ROIs) for further classification and diagnosis.

Acknowledgments

Reference

[1] J.A. Noble, D. Boukerroui, Ultrasound image segmentation: a survey, IEEE Trans. Med. Imag. 25 (8) (2006) 987–1010.

[3] E.A. Ashton, K.J. Parker, Multiple resolution Bayesian segmentation of ultrasound images, Ultrason. Imag. 17 (1995) 291–304.

[4] D. Boukerroui, O. Basset, A. Baskurt, G. Gimenez, A multiparametirc and multiresolution segmentation algorithm of 3-D ultrasonic data, IEEE Trans. Ultrason. Ferroelectrics Freq. Control 48 (1) (2001) 64–77.

[5] G. Xiao, M. Brady, J.A. Noble, Y. Zhang, Segmentation of ultrasound B-mode images with intensity inhomogeneity correction, IEEE Trans. Med. Imag. 21 (1) (2002) 48–57.

[6] D. Boukerroui, A. Baskurt, J.A. Noble, O. Basset, Segmentation of ultrasound images multiresolution 2D and 3D algorithm based on global and local statistics, Pattern Recognition Lett. 24 (2003) 779–790.

[7] X. Hao, C.J. Bruce, C. Pislaru, J.F. Greenleaf, Segmenting high-frequency intracardiac ultrasound images for myocardium into infarcted, ischemic and normal regions, IEEE. Trans. Med. Imag. 20 (12) (2001) 1373–1383.

[8] A. Madabhushi, D.N. Metaxas, Combining low-, high-level and empirical domain knowledge for automated segmentation of ultrasonic breast lesions, IEEE Trans. Med. Imag. 22 (2) (2003) 155–169.

[9] P. Abolmaesumi, M.R. Sirouspour, An interacting multiple model probabilistic data association filter for cavity boundary extraction from ultrasound images, IEEE Trans. Med. Imag. 23 (6) (2004) 772–784.

[10] C. Kotropoulos, I. Pitas, Segmentation of ultrasonic images using support vector machines, Pattern Recognition Lett. 24 (2003) 715–727.

[11] Y. Zhan, D. Shen, Deformable segmentation of 3-D ultrasound prostate images using statistical texture matching method, IEEE Trans. Med. Imag. 25 (3) (2006) 256–272.

[12] H.M. Wu, H.H. Lu, Iterative sliced inverse regression for segmentation of ultrasound and MR images, Pattern Recognition 40 (2007) 3492–3502.

[13] M. Mulet-Parada, J.A. Noble, 2D+T acoustic boundary detection in echocardiography, Med. Image Anal. 4 (1) (2000) 21–30.

[14] Y.L. Huang, D.R. Chen, Watershed segmentation for breast tumor in 2-D sonography, Ultrasound Med. Biol. 30 (5) (2004) 625–632.

[15] C.M. Chen, Y.H. Chou, C.S.K. Chen, J.Z. Cheng, Y.F. Ou, F.C. Yeh, K.W. Chen, Cell-competition: a new segmentation algorithm for multiple objects with irregular boundaries in ultrasound images, Ultrasound Med. Biol. 31 (12) (2005) 1647–1664.

[16] M.R. Cardinal, J. Meunier, G. Soulez, R. Maurice, E. Therasse, G. Cloutier, Intravascular ultrasound image segmentation: a three-dimensional fast marching method based on gray level distributions, IEEE Trans. Med. Imag. 25 (5) (2006) 590–601.

[17] G.I. Sanchez-Ortiz, G.J.T. Wright, N. Clarke, J. Declerck, A. Banning, J.A. Noble, Automated 3D echocardiography analysis compared with manual delineation and MUGA, IEEE Trans. Med. Imag. 21 (9) (2002) 1069–1076.

[18] C.M. Chen, H.H.S. Lu, Y.C. Lin, An early vision-based snake model for ultrasound image segmentation, Ultrasound Med. Biol. 26 (2) (2000) 273–285.

[19] D.R. Chen, R.F. Chang, W.J. Wu, W.K. Moon, W.L. Wu, 3-D Breast ultrasound segmentation using active contour model, Ultrasound Med. Biol. 29 (7) (2003) 1017–1026.

[20] A. Sarti, C. Corsi, E. Mazzini, C. Lamberti, Maximum likelihood segmentation of ultrasound images with Rayleigh distribution, IEEE Trans. Ultrason. Ferroelectrics Freq. Control 52 (6) (2005) 947–960.

[21] G. Slabaugh, G. Unal, T. Fang, M. Wels, Ultrasound-specific segmentation via decorrelation and statistical region-based active contours, CVPR, 2006.

[22] H. Mao, H. Liu, P. Shi, Neighbor-constrained active contours without edges, CVPR, 2008.

[23] C.B. Burckhardt, Speckle in ultrasound B-mode scans, IEEE Trans. Sonics Ultrason. 25 (1978) 1.

[24] R.F. Wagner, S.W. Smith, J.M. Sandrik, H. Lopez, Statistics of speckle in ultrasound B-scans, IEEE Trans. Sonics Ultrason. 30 (3) (1983) 156–163.

[25] Y.J. Yu, S.T. Acton, Speckle reducing anisotropic diffusion, IEEE Trans. Image Process. 11 (11) (2002) 1260–1270.

[26] Y. Chen, R.M. Yin, R. Flynn, S. Broschat, Aggressive region growing for speckle reduction in ultrasound images, Pattern Recognition Lett. 24 (2003) 677–691.

[27] O.V. Michailovich, A. Tannenbaum, Despeckling of medical ultrasound images, IEEE Trans. Ultrason. Ferroelectrics Freq. Control 53 (1) (2006) 64–78.

[28] S. Osher, J.A. Sethian, Front propagating with curvature dependent speed: algorithms based on Hamilton Jacobi formulation, J. Comput. Phys. 79 (1988) 12–49.

[29] R. Malladi, J.A. Sethian, B.C. Vemuri, Shape modeling with front propagation: a level set approach, IEEE Trans. Pattern Anal. Mach. Intell. 17 (2) (1995) 158–175.

[30] N. Lin, W. Yu, J.S. Duncan, Combinative multi-scale level set framework for echocardiographic image segmentation, Med. Image Anal. 7 (4) (2003) 529–537.

[31] R.F. Chang, W.J. Wu, W.K. Moon, D.R. Chen, Automatic ultrasound segmentation and morphology based diagnosis of solid breast tumors, Breast Cancer Res. Treat. 89 (2) (2005) 179–185.

[32] M. Kass, A. Witkin, D. Terzopoulos, Snakes: active contour models, Int. J. Comput. Vision 1 (1988) 321–331.

[33] V. Caselles, R. Kimmel, G. Sapiro, On geodesic active contours, Int. J. Comput. Vision 22 (1) (1997) 61–79.

[34] T.F. Chan, L.A. Vese, Active contours without edges, IEEE Trans. Image Process. 10 (2) (2001) 266–277.

[35] C. Li, C.Y. Kao, J.C. Gore, Z.H. Ding, Minimization of region-scalable fitting energy for image segmentation, IEEE Trans. Image Process. 17 (10) (2008).

[36] P. Martin, P. Refregier, F. Goudail, F. Guerault, Influence of noise model on level set active contour segmentation, IEEE Trans. Pattern Anal. Mach. Intell. 26 (6) (2004) 799–803.

[37] D. Cremers, A review of statistical approaches to level set segmentation: integrating colors, texture, motion and shape, Int. J. Comput. Vision 72 (2) (2007) 192–215.

[38] M.J. Ledesma-Carbayo, J. Kybic, M. Desco, A. Santos, M. S'uhling, P. Hunziker, M. Unser, Spatio-temporal non-rigid registration for ultrasound cardiac motion estimation, IEEE Trans. Med. Imag. 24 (9) (2005).

[39] R.C. Gonzales, R.E. Woods, Digital Image Processing, second ed, Prentice-Hall, New York, 2002.

[40] C. Li, C. Xu, C. Gui, M.D. Fox, Level set evolution without reinitialization: a new variational formulation, Proc. IEEE Conf. Comput. Vision Pattern Recognition 1 (2005) 430–436.

[41] F. Sattar, L. Floreby, G. Salomonsson, B. Lövström, Image enhancement based on a nonlinear multiscale method, IEEE Trans. Image Process. 6 (1997) 888–895.

[42] A. Achim, A. Bezerianos, P. Tsakalides, Novel Bayesian multiscale method for speckle removal in medical ultrasound images, IEEE Trans. Med. Imag. 20 (8) (2001) 772–783.

[43] N. Paragios, R. Deriche, Geodesic active contours and level sets for the detection and tracking of moving objects, IEEE Trans. Pattern Anal. Mach. Intell. 22 (3) (2000) 266–280.

[44] V. Chalana, Y. Kim, A methodology for evaluation of boundary detection algorithms on medical images, IEEE Trans. Med. Imag. 16 (5) (1997) 642–652.

[45] C. Bouma, W. Niessen, K. Zuiderveld, E. Gussenhoven, M. Viergever, Evaluation of segmentation algorithms for intravascular ultrasound images, Visualization Biomed. Comput. (1996) 203–212.

[46] J. Perona, J. Malik, Scale-scape and edge-detection using anisotropic diffusion, IEEE Trans. Pattern Anal. Mach. Intell. 12 (7) (1990) 629–639.

[47] R.N. Czerwinski, D.L. Jones, W.D. O' Brien, Detection of lines and boundaries in speckle images—application to medical ultrasound, IEEE Trans. Med. Imag. 18 (2) (1999) 126–136.

[48] N. Otsu, A threshold selection method form gray-level histograms, IEEE Trans. Syst. Man Cybern. 9 (1) (1979) 62–66.

[49] J.K. Udupa, V.R. LeBlanc, H. Schmidt, C. Imielinska, P.K. Saha, G.J. Grevera, Y. Zhuge, L.M. Currie, P. Moholt, Y. Jin, A methodology for evaluating image segmentation algorithms, Proc. SPIE 2 (2002) 266–277.

[50] G.W. Williams, Comparing the joint agreement of several raters with another rater, Biometrics 32 (1976) 619–627.

[51] J.L. Rogers, W.A. Nicewander, Thirteen ways to look at the correlation coefficient, Am. Stat. 42 (1988) 59–66.

About the author—BO LIU received the B.S. degree in Computer Science and Technology from Northeast Forestry University (China) in 2004 and the M.S. degree in Computer Application from Harbin Institute of Technology (China) in 2006. He is now a Ph.D Candidate (Supervisor: H.D. Cheng) in Pattern Recognition and Intelligent Systems at Harbin Institute of Technology. His current research interests include medical image processing, pattern recognition and artificial intelligence.

About the author—H.D. CHENG received Ph.D. degree in Electrical Engineering from Purdue University, (Supervisor: Prof. K.S. Fu), West Lafayette, IN, 1985. Dr. Cheng is an Adjunct Professor and Doctorial Supervisor of Harbin Institute of Technology, and he is a Full Professor, Department of Computer Science, and an Adjunct Full Professor, Department of Electrical Engineering, Utah State University, Logan, Utah.

Dr. Cheng has published more than 200 technical papers and is the co-editor of the book, Pattern Recognition: Algorithms, Architectures and Applications (World Scientific Publishing Co., 1991). His research interests include image processing, pattern recognition, computer vision, artificial intelligence, medical information processing, fuzzy logic, genetic algorithms, neural networks, parallel processing, parallel algorithms, and VLSI architectures.

Dr. Cheng is the general chair of the 9th Joint Conference on Information Sciences (JCIS2006), was the general chair of the 8th Joint Conference on Information Sciences (JCIS2005) general chair and program chair of the sixth International Conference on Computer Vision, Pattern Recognition and Image Processing (CVPRIP2005), and was the general chair and program chair of the Fifth International Conference on Computer Vision, Pattern Recognition and Image Processing (CVPRIP2003), 2003, and was the general chair and program chair of the Fourth International Conference on Computer Vision, Pattern Recognition and Image Processing (CVPRIP'2002), 2002, the general chair and program chair of the Third International Conference on Computer Vision, Pattern Recognition and Image Processing (CVPRIP'2000), 2000, the general chair and program chair of the First International Workshop on Computer Vision, Pattern Recognition and Image Processing (CVPRIP'98), 1998, and the Program Co-Chairman of Vision Interface '90, 1990. He served as program committee member and session chair for many conferences, and as reviewer for many scientific journals and conferences.

Dr. Cheng is also an Associate Editor of Pattern Recognition and an Associate Editor of Information Sciences.

About the author—JIANHUA HUANG, associate professor of Harbin Institute of Technology. He received B.S. degree at HIT in 1989, M.S. degree at HIT in 1992 and Ph.D. degree at HIT in 2007. His research interests include artificial intelligence, pattern recognition, image processing, text recognition in nature scene and intelligent motion analysis of human beings.

About the author—JIAWEI TIAN, professor of Department of Ultrasound, Second Affiliated Hospital of Harbin Medical University. She received bachelor's degree in Clinical Medicine from Harbin Medical University in 1980 and Master's degree in Imaging and Nuclear Medicine from China Medical University in 1993. She is a very experienced radiologist, and has worked in this field more than 27 years. Professor Tian has published more than 92 medical papers. Her recent research interests include: ultrasonic diagnosis and intervene treatment for superficial organs and cardiovascular diseases.

About the author—XIANGLONG TANG, professor of Harbin Institute of Technology, director of pattern recognition research center of HIT, senior member of China Computer Foundation. He received B.S. degree at HIT in 1982, M.S. degree at HIT in 1986 and Ph.D. degree at HIT in 1995. Dr. Tang has published more than 80 papers in the fields of image processing, pattern recognition and artificial intelligence. His recent research interests include: medical imaging, intelligent motion analysis of human beings, hand-writing character recognition and pattern recognition.

About the author—JIAFENG LIU, received his B.E degree in 1990 and Ph.D. degree in 1996 from Harbin Institute of Technology. He is currently an associate professor at Harbin Institute of Technology. His current research interests include pattern recognition, image processing and computer vision.